Journal of Science: Advanced Materials and Devices 9 (2024) 100695

Contents lists available at ScienceDirect

Journal of Science: Advanced Materials and Devices

journal homepage: www.elsevier.com/locate/jsamd

Investigating the effect of Zr content on electrochemical and tribological properties of newly developed near β-type Ti-alloys (Ti–25Nb-xZr) for biomedical applications

Mamoun Fellah [a,**], Naouel Hezil [b], Dikra Bouras [c], Nabila Bouchareb [b], Alejandro Perez Larios [d], Aleksei Obrosov [e,*], Gamal A. El-Hiti [f], Sabine Weiß [e]

[a] Mechanical Engineering Department, Khenchela University, 40004, Algeria
[b] Matter Sciences Department, Khenchela University, 40004, Algeria
[c] Faculty of Science and Technology, University of Souk-Ahras, Algeria
[d] Nanocatalysis Research Laboratory, Department of Engineering, Centro Universitario de Los Altos, University of Guadalajara, Tepatitlán de Morelos, Jalisco, Mexico
[e] Brandenburg University of Technology Cottbus-Senftenberg, Konrad-Wachsmann-Allee 17, Cottbus, 03046, Germany
[f] Department of Optometry, College of Applied Medical Sciences, King Saud University, Riyadh, 11433, Saudi Arabia

ARTICLE INFO

Keywords:
Ti-Nb-Zr alloys
Nanobiomaterials
Tribological behavior
Corrosion
Ringer's solution
Biomedical applications

ABSTRACT

In order to create alloys with exceptional properties for orthopedic uses, this study focuses on the impact of zirconium (Zr) content on the structural, electrochemical, and tribological qualities of nanostructured Ti–25Nb-xZr [x = 5, 10, 15, 20, 25, and 30 atomic (at.) %] alloys. The structural evolution was investigated using XRD and SEM techniques. The mechanical characteristics of the produced alloys, including Vickers hardness and Young's modulus, were measured. In addition, the corrosion tests were performed using the OCP, EIS, and PD methods in Ringer's solution within the independent pH range at 37 °C. A ball-on-disc tribometer was used to investigate the tribological behavior of the alloys under various loads and wet conditions using the Ringer solution. It has been verified that Zr content (at. %) in the alloys had an impact on their morphologies, structural evolution, and mechanical characteristics. According to the morphological analysis, the particle and crystallite size decreases with increasing Zr content. Young's modulus and Vickers hardness show the same tendency. The EIS data demonstrated that a single passive film formed on the alloy surfaces, and the addition of Zr enhanced the corrosion resistance of the passive films. The polarization curves demonstrate that the alloys had low corrosion current densities and large passive areas without the passive films disintegrating. Likewise, the inclusion of Zr resulted in a reduction in the corrosion and passive current density values. All of these results suggested that the titanium alloys exhibit a more noble electrochemical activity caused by Zr. From the tribological perspective, it was found that the friction coefficient of the alloys reduced with increasing Zr content.

1. Introduction

The mechanical properties of bones can deteriorate due to abnormal endogenous self-healing mechanisms or excessive stress, osteoarthritis, degenerative diseases, and trauma [1–5]. The creation of artificial biomaterials that can be surgically implanted in the proper morphology to enable the restoration of damaged systems is one of the solutions to these problems [1–5]. The biocompatibility of these materials is a significant problem, as tissue neoformation with posterior characteristics develops on the implanted devices [6]. Therefore, these basic characteristics of the implanted materials, such as their microstructure, morphology, content, and organic properties, dictate their efficiency [2].

Therefore, the materials produced must be biocompatible, have high corrosion resistance, and exhibit the correct mechanical properties to be considered excellent candidates for biomedical applications [7,8]. Numerous biomaterial alloys with significantly improved characteristics have been created in the last few decades. However, most of these newly

Peer review under responsibility of Vietnam National University, Hanoi.
* Corresponding author.
** Corresponding author.
E-mail addresses: mamoune.fellah@univ-khenchela.dz (M. Fellah), aleksei.obrosov@b-tu.de (A. Obrosov).

https://doi.org/10.1016/j.jsamd.2024.100695
Received 20 January 2024; Received in revised form 23 February 2024; Accepted 29 February 2024
Available online 7 March 2024

discovered materials and alloys are dense, which causes a biomechanical mismatch that can cause harmful responses and a number of other issues. The three most widely used metallic alloys in modern times are stainless steel, Co alloys, and Ti alloys [8–10]. However, these materials have shown a tendency to fail after extended usage for a number of reasons, including poor corrosion resistance and excessive Young's modulus [1–4].

Actually, titanium alloys have drawn much interest because of their possible applications [11] due to their exceptional corrosion resistance. They replace conventional materials like SS 316 L and Co–Cr alloys in the majority of biomedical applications because they offer significant advantages over those materials [12]. Numerous studies on the fabrication of Ti alloys with various elements are found in the literature [13]. However, the most commonly utilized Ti–6Al–4V alloy is harmful to human health and may cause mutagenic cytology and hypersensitive reactions [14,15]. Therefore, Ti–Al–Nb and Ti–Al–F alloys were developed [10–12] to replace the V in the titanium alloys. These alloys have extremely high Young's modules, which causes stress shielding due to significant variations in mechanical characteristics compared to the ones of bones [16].

The development of titanium alloys, which consist of strengthening and stabilizing alloying elements like Nb, Mo, Ta, and W [1–16], was forced to overcome this challenge further. Numerous structures, such as Ti–Zr–Al–V, Ti–Zr or Ti–Mo have been suggested [17–20]. However, each of these structures has its benefits and drawbacks. For example, it was shown that Mo causes significant compatibility problems with human tissue in the Ti–Mo system [18,20].

Based on current research, the elastic modulus of Ti- (20–50 at. %) Nb alloys is approximately 61 GPa [21,22]. Furthermore, an increase in Nb content tends to stabilize the titanium β-phase while lowering the Young's modulus of these alloys [21–24]. For demanding biomedical applications, a metastable Ti–33Nb–4Sn alloy with good characteristics has recently been developed [25]. Since Zr was discovered as a biocompatible and neutral alloying element for titanium [7,8,26], Ti–Nb–Zr alloys with superior qualities were created. The inclusion of Zr improves the biocompatibility of the alloys. It decreases the production of undesirable phases, such as the omega phase (ω) [27,28], which is well-known to increase the elastic modulus [29].

Additionally, it was shown that the Zr addition enhanced the superelastic behavior and shape memory effects (SME) of the Ti–Nb system, which is advantageous for biomedical applications [30]. Despite it being one of the controlling elements that determine many characteristics of the alloy, there are – to the authors' best knowledge – few studies in the literature that published the effect of Zr addition on the structural and tribological behaviors of Ti–Nb–Zr structures [20,21]. Therefore, these issues, together with the mechanical and corrosion characteristics of nanostructured Ti–25Nb-xZr alloys with (x = 5, 10, 15, 20, 25, 30) formed using ball milling were investigated for the first time in the current work.

2. Experimental

2.1. Samples preparation

The ternary Ti–25Nb-xZr (x = 5, 10, 15, 20, 25, and 30 at. %) alloys are manufactured using highly pure powders of Ti (99.98 %), Nb (99.97 %), and Zr (99.98 %) acquired through the SIGMA-Aldrich society (Fig. 1). Their compositions and properties are presented in Table 1.

A ball mill type (Pulverisette P7) was used to create uniform powder combinations. 80 mL hardened metallic vials were milled with 10 mm diameter balls with BPR of 20:1. The grinding cycle takes 30 min of grinding at 400 rpm, followed by 30 min of rest.

The milled powders were processed by utilizing a HIP process at 300 MPa to form cylindrical samples with a diameter of 13 mm. After that, the HIPed specimens were sintered in a high vacuum furnace operating at 10^6 bars for 4 h at 1250 °C with a heat/cool rate of 12 °C.min^{-1} (Fig. 1).

2.2. Structural characterization

The particle morphology was evaluated using an SEM (SEM, Zeiss

Table 1
Characteristics of the elemental powders employed for manufacturing the Ti–25Nb–xZr alloys [22].

	Ti	Nb	Zr
Particle size	<100 μm		
O (at.%)	0.057	0.314	0.212
Fe (at.%)	0.0052	0.00034	0.0002
N (at.%)	0.0015	0.0018	0.00330
H (at.%)	0.005	0.00023	0.00090
C (at.%)	0.04	0.0074	0.001
Atomic radius (nm)	0.148	0.145	0.161
Melting temperature (°C)	1668	2477	1855

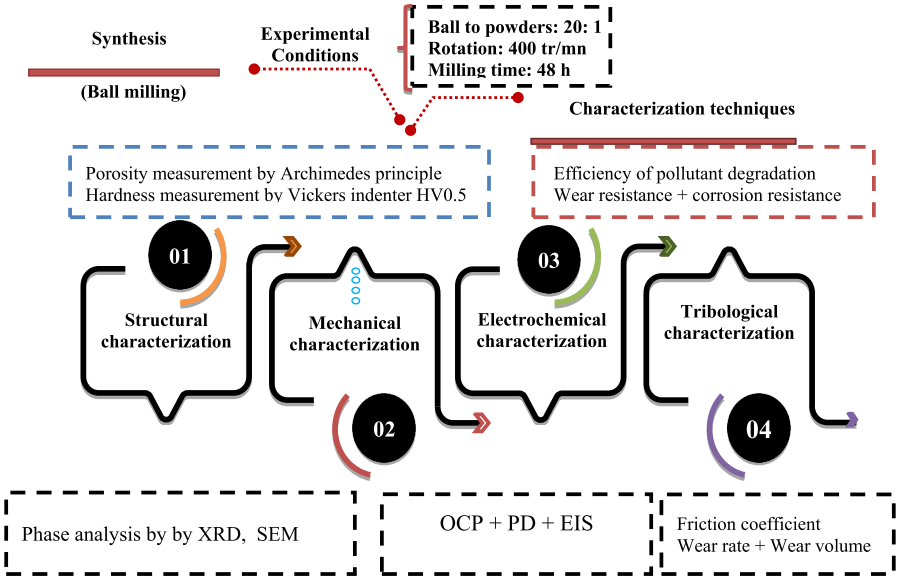

Fig. 1. Sample production process and characterization techniques.

DSM 960A at a voltage of 20 kV) (Fig. 2). A Mini Flex600 X-ray diffractometer from Rigaku Corporation was used to identify the various stages in the samples. The specimens' hardness was measured with a Zwick ZHV2.0 outfitted with a Vickers diamond indenter.

2.3. Electrochemical characterization

The electrochemical analysis was conducted utilizing a standard corrosion 3-electrode cell; the platinum (Pt) was used as the counter electrode, (SCE) saturated calomel electrode as the reference electrode, and the working electrode (WE) was the Ti–25Nb-xZr samples. To imitate human body fluid, Ringer solution, with a pH value of roughly 7.4, was used as an electrolyte (Table 2). All studies were carried out with a Solartron 1287 potentiostat and a Solartron 1260 frequency response analyzer equipment (ENSAM Lille, France) at 37 °C (Fig. 3).

EIS measurements were done using a frequency range of (10^{-2}-10^{5} Hz) and a potential amplitude of 10 mV in an open-circuit potential. Zview 2.1b was used as a suitable model for quantification of the equivalent circuit in order to provide the quantitative data for the discussion of the experimental EIS results. To ensure that the steady-state condition was reached, the tests were started after 1 h of holding time.

Using a Solartron 1287 potentiostat, initial studies on the potentiodynamic properties of the Ringer solution were carried out. The scanning rate ranged from −500 to +2400 $mV_{/SCE}$, with a potential of 1 mV/s. The polarization curves were produced using a data acquisition system (*Cview. 2 version*). The potential and the corrosion rate were determined using Tafel plots, utilizing both cathodic and anodic branches.

2.4. Tribological characterization

In compliance with the ISO 7148–1:2012, ASTMG 99, and ASTM G133-95 standards, tribological tests were performed utilizing a

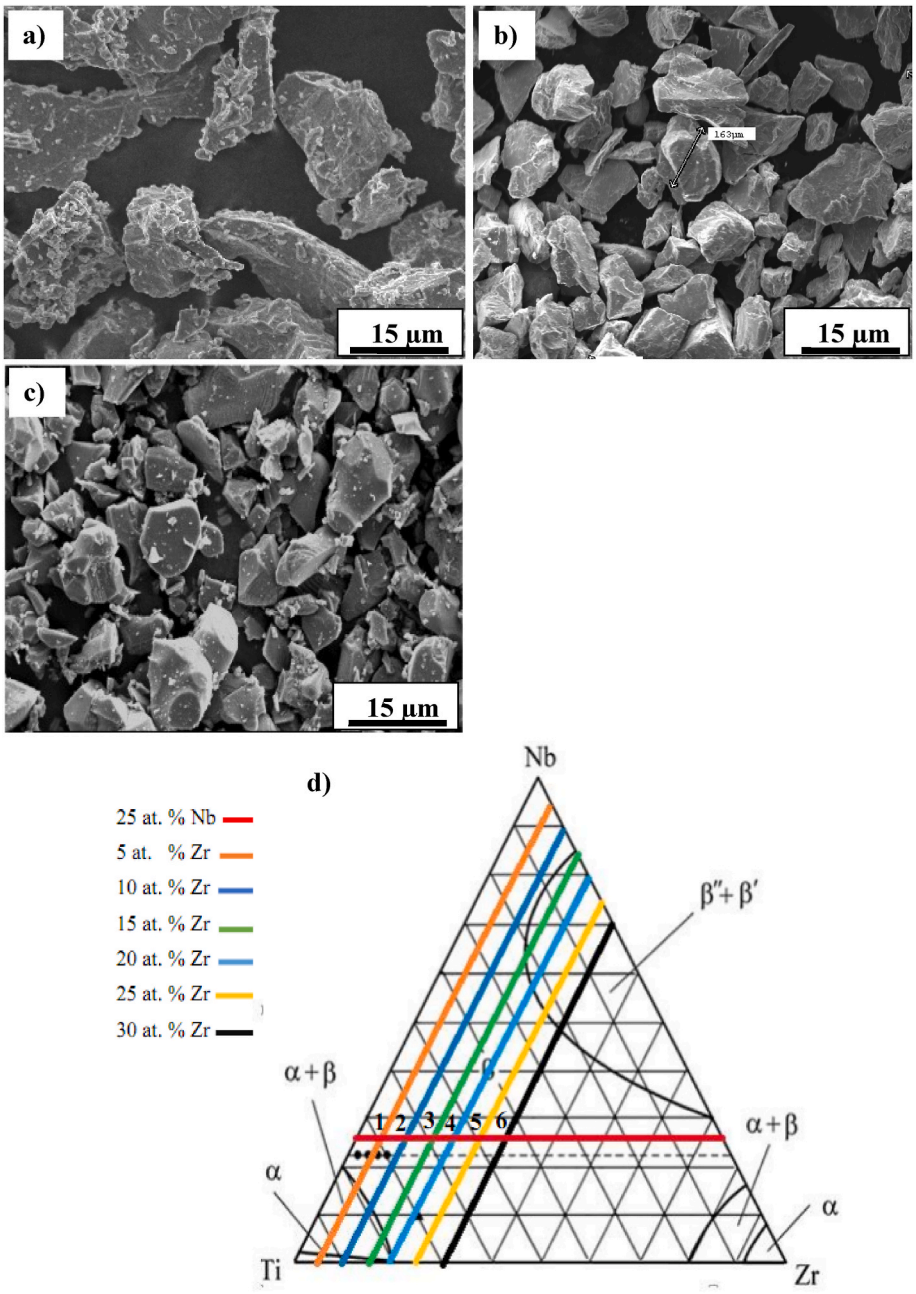

Fig. 2. SEM images of the particles of the pure powders: a)-Ti, b)-Nb, c)-Zr. and d)- phase diagram of Ti–Nb–Zr system at 500 °C [17].

Table 2
Ringer solution's chemical composition [9].

Components	NaCl	$CaCl_2$	KCl	$C_6H_{12}O_6$	$C_8H_{18}N_2O_4S$	(Glucose)	Hepes Buffer
$g.l^{-1}$	6.44	0.26	0.20	1.82	2.40	/	Hepes Buffer

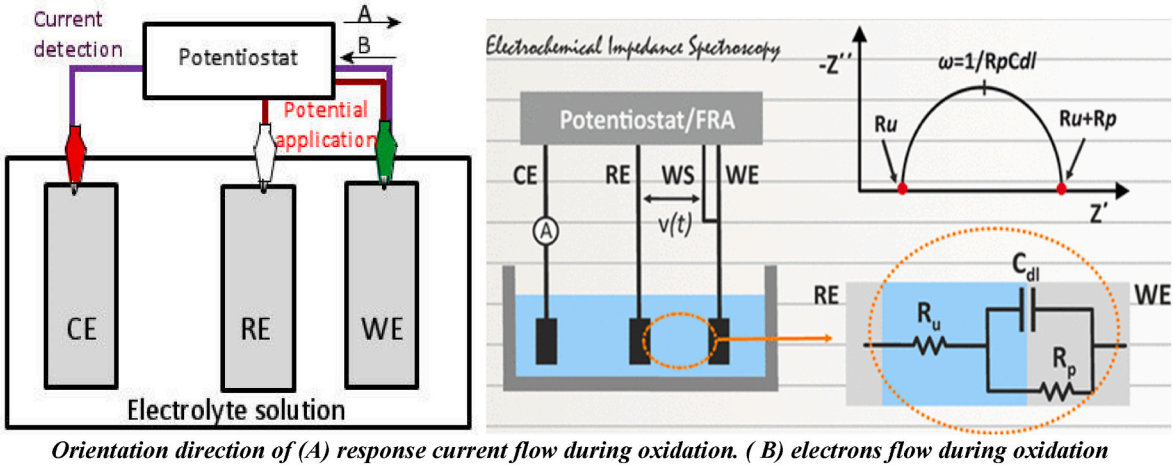

Fig. 3. Scheme of an experimental 3-electrode electrochemical cell.

tribometer (Tribotester) with a ball-on-plate configuration (Fig. 4) under wet conditions with Ringer solution as simulated body fluid [9]. The experiments were conducted using a 6 mm alumina ball (Al_2O_3) with an elastic modulus, hardness, and density of (E = 324 GPa, $HV_{0.02}$ = 2454, and = 3.98 g cm^3 correspondingly) as the counterface, sliding at a speed of 15 mm/s.

3. Results and discussion

3.1. Structural characterization

3.1.1. Morphological characterization

The effect of different Zr content on the microstructure of Ti–25Nb-xZr powders after mechanical milling is presented in Fig. 5. The micrographs distinctly demonstrate the gradual changes in the shape and size of the particles at varying Zr content levels (Zr = 5, 10, 15, 20, 25, and 30 at. %). In accordance with the typical properties of the milling process, the size of the milled powder particles first increased and subsequently dropped [31]. It may be suggested that the alloys' grain sizes were refined with Zr addition [32].

The agglomerate structure and particle size distribution displayed in the micrographs suggest that the initial substrate powders were continuously subjected to cold welding and fracture. As reported in a previous study, these agglomerates or rising particle sizes are the result of the plastic deformation that was induced and the increased temperature during mechanical milling [33]. The numerous nanoparticles in the milled powder were created by the continuous plasticization, hardening, breaking, and cold-welding of a metal powder due to ball and extrusion impacts [34].

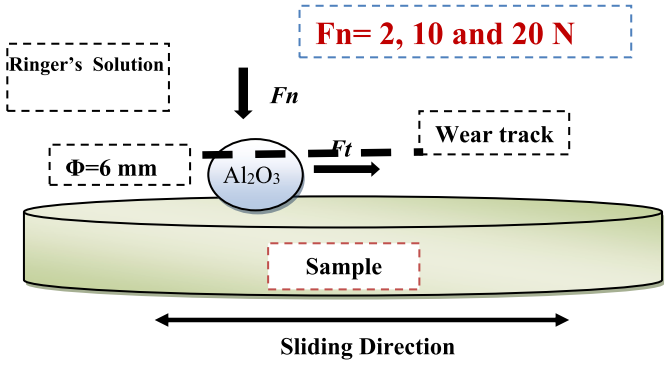

Fig. 4. Scheme of a ball-on-disc type oscillating Tribotester.

With 5 at. % Zr content (Fig. 5a), the powder charge had at least 15% by volume of the ductile phase of the alloys. In this case, the particle size was relatively distributed uniformly, and particles were agglomerated, which got smaller and rounder as the proportion of Zr increased. Particle size increases as a result of the particles' ability to bind with one another on the newly formed surfaces [35]. According to Fig. 5 b-d, samples with 10, 15, and 20 at. %, respectively, show that the fatigue mechanism causes the deformation to continue and the particles to harden and occasionally fracture.

When there are no substantial agglomeration dynamics, the fragments formed by this mechanism can further reduce in size to reach the nanometric scale [36,37]. The grinding bodies' constant impact continuously refines the particle structure, but the particle size stays constant [38]. Consequently, the proportion of each particle's lamellar structures increases, and interlamellar distances decrease [39].

For specimens with 25 and 30 at. % of Zr content (Fig. 5 e and f), the range of particle sizes is limited at this point because larger particles typically divide into smaller ones. In contrast, smaller pieces tend to agglomerate and grow larger until they reach the micrometer scale. The crystallites' size is progressively reduced to nanometric dimensions, and the interlamellar distance is smaller between milling for a few minutes to an hour [40]. To summarize, the shape of the particles that make up the Ti–25Nb-xZr compound after the milling process has the sizes and shapes shown in Fig. 5.

3.1.2. XRD analysis

The XRD spectra of the milled powders are displayed in Fig. 6a. The XRD pattern for the sample with 5 at. % Zr reveals the presence of β and α phases. The α-Ti phase is represented by the peaks located near $2\Theta \approx$ 36.7, 40, 64, 78, and 110°, and the β-Ti phase is represented by the peaks located at $2\Theta \approx$ 41.8, 54.5, 72.4, 87, and 115°.

The intensity of the peaks related to the α and β-Ti phases, which are

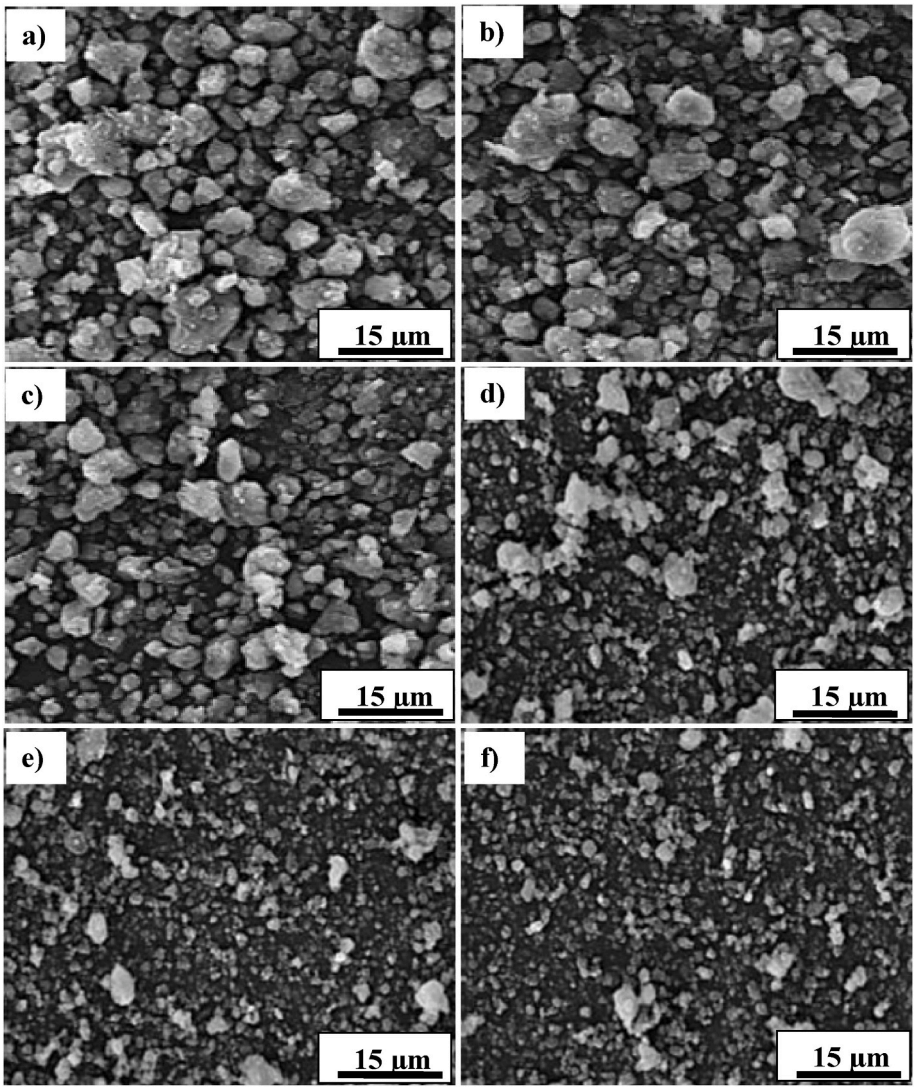

Fig. 5. SEM micrograph of Ti–25Nb-XZr as a function of the Zr content milled for 18 h..

positioned between 50° and 90°, dropped significantly with increasing Zr content, to the point where they nearly vanished in the sample with 30 at. % Zr. It is also valid for the peak positioned at $2\Theta = 110°$. However, the neighboring peak at $2\Theta = 110°$ retained its intensity but shifted to lower 2Θ values. Hence, β-Ti peaks disappeared, which can be ascribed to the excessive Zr content, suggesting that α-Ti is predominant.

The intense peaks near $2\Theta \approx 36.7$, 40, and 41.8° also shifted to lower angles, as shown in Fig. 6b, with a remarkable reduction in intensity. As the Zr content increased, a broadening of the peak profile occurred, as indicated clearly in Fig. 6b, resulting from milling-induced plastic deformation and particle size refinement, which caused a change in the cell parameters. Concurrently, a peak displacement to lower angles, attributed to crystal structure distortion and a variation in the Ti lattice parameters, most likely as a lattice strain consequence caused by the Nb and Zr insertion in the Titanium matrix [1,2], can be observed in Fig. 6b.

It is crucial to note that the increase in Zr content causes a more substantial shift compared to other processing parameters, such as sintering temperature [1] and Milling time [3]. It can be explained mainly by the Zr content: excessive amounts of Zr, like 25 or 30 at. %, initiate severe distortion of the Ti lattice. Comparing the atomic radii of Ti with 0.147 nm, Nb with 0.144 nm, and Zr with 0.160 nm, the Zr atom is much larger than both Ti and Nb atoms. Hence, during phase transition, the insertion of Zr in the Titanium matrix produces significant distortion.

3.1.3. Lattice parameters, microstrain, and crystallite size evolution

Fig. 7 illustrates the progression of the lattice parameters, microstrain, and crystallite size of the Ti–25Nb-xZr systems as a function of the Zr content (at. %). A substantial increase in the lattice parameters (a_β) from 3.314 to 3.334 Å was observed with the addition of Zr, as shown in Fig. 7a. It corresponds to a cell extension by 1.07% in volume. The lattice parameter values of the Ti–25Nb-xZr samples with the addition of Zr were similar to those presented previously [42].

Obviously, the increasing Zr content decreased the crystallite size from 65 nm at 5% Zr to the lowest value of 31 nm at 30 at. % Zr. Conversely, the mean values of microstrain grew from 0.31 to 0.94% when the Zr content increased from 0 to at. 35%. The above conclusions and observations can be attributed to phase transition resulting in induced stress and matrix expansion. In agreement with the binary Ti–Nb alloys [22], the inclusion of Nb increases the β phase lattice parameter.

Fig. 7b illustrates the influence of Zr addition on the crystallite size. By adding 30 at.% Zr, a fine crystallite size of less than 31 nm is achieved. The reduction in the diffusion coefficient due to the addition of Zr can be responsible for the refinement of the crystallite size. The nanocrystalline allows alloys with high strength, polishability, and good workability to be produced [21].

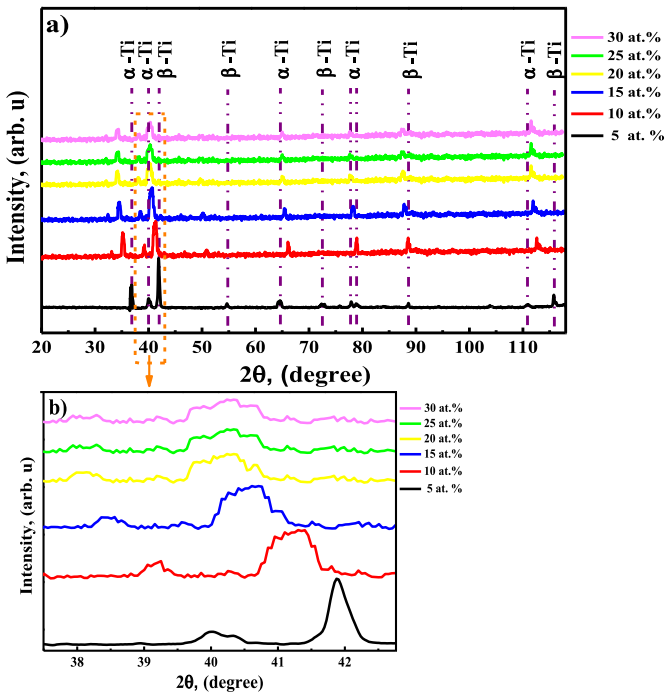

Fig. 6. (a) XRD Diagrams of the Ti–25Nb-XZr samples alloys, (b) Enlarged presentation of the peaks shift to lower angles.

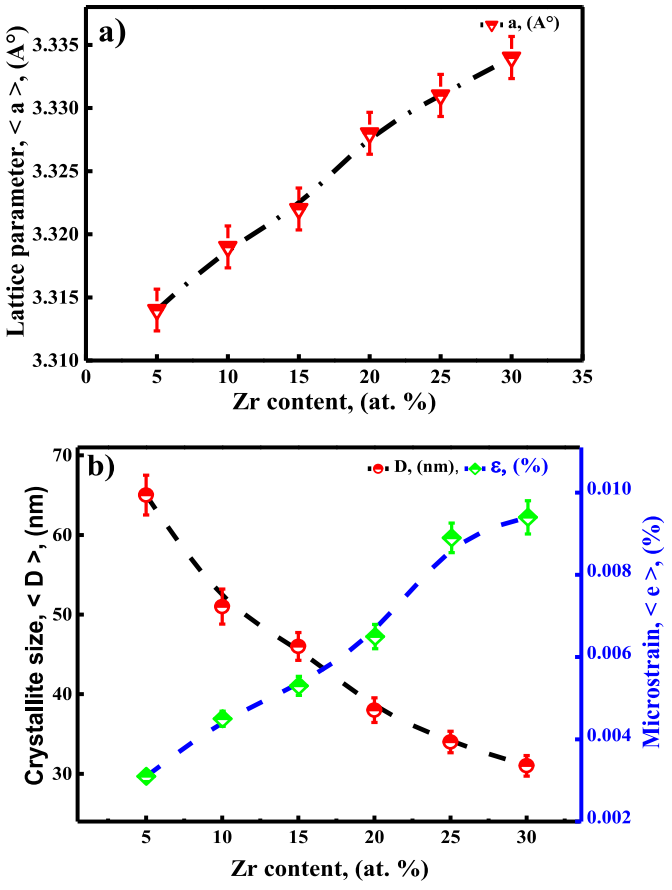

Fig. 7. Evolution of: a) Lattice parameters, and b) Crystallite size and microstrain of ternary Ti–25Nb-xZr samples.

3.2. Mechanical characterization

3.2.1. Porosity and relative density

Fig. 8 shows the evolution of relative density and porosity of compacted Ti–25Nb-xZr specimens with Zr (at. %) added. The porosity (%) reduced from 0.19 to 0.16, 0.10, 0.009, and 0.007 (%), and the pore size decreased from 58 to 53, 44, 41, and 38 nm, with the Zr content increasing from 5 to 10, 15, 20, 25, and 30 at. %, respectively. The results show that the density values increase with Zr addition in such a way that alloys with 30 at. % Zr present a higher value of ≈91.3% than the alloys with 5, 10, 15, 20, and 25 at. % Zr with values of 72, 81, 86, and 90%, respectively.

As reported in the literature [16], the Zr addition to the Ti alloys acts as an element that hinder the improvement of hardness. The larger amount of Nb and Zr seems to eliminate the α phase so that the Ti–Nb–Zr system becomes more susceptible to indentation and, therefore, has a lower hardness [26]. This result suggests that Ti–Nb–Zr may be particularly ductile with increasing Zr content and should, therefore, exhibit better forming compared to Ti–25Nb-xZr systems with low amounts of Zr (0 and 5 at. % Zr).

3.2.2. Young's modulus and hardness characterizations

The results of elastic modulus and microhardness obtained by micro indentation of the sintered and compacted Ti–25Nb-xZr samples with various Zr additions (5, 10, 15, 20, 25, and 30 at. %) are displayed in Fig. 9. Young's modulus (elastics modulus) and hardness reduce with the addition of Zr, which results from the suppression of the precipitation phase (ω) and the increase of the β lattice parameter upon reaching 20 and 30 at. % Zr, hardness, and Young's modulus stabilize at a low level.

Interatomic forces influence the elastic modulus and decrease when the interatomic distance increases. The addition of 25 at.% Zr lowers the Young's modulus value significantly. The trends in Fig. 9 show that the samples with 5 at. % Zr have higher values of 300 HV and 76 GPA than the samples with 30 at. % Zr with values of 233 HV and 60 GPa for $HV_{0.02}$ and E, respectively. Elastic modulus should be close to that of human bone for use in biomedical applications [16].

Therefore, the Ti–25Nb–25Zr system can be an appropriate candidate for biomedical applications. For Nb >22%, a stable bcc (β) phase occurs in the Ti–Nb system. Thus, Ti–25Nb was found to be the best composition (with E∼82 GPa). Furthermore, the Zr element is chosen to be added to the Ti25–Nb composition, primarily to reduce the formation energy of the β-phase and to decrease its Elastics modulus [16]. The Elastics modulus (E∼ 61 GPa) is correspondingly low for the composition Ti–25Nb–30Zr.

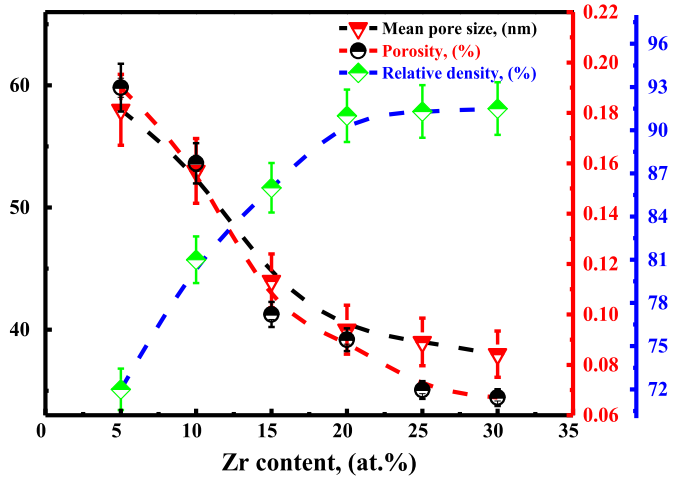

Fig. 8. Evolution of Porosity and the relative density of Ti–25Nb-xZr versus Zr content (at. %).

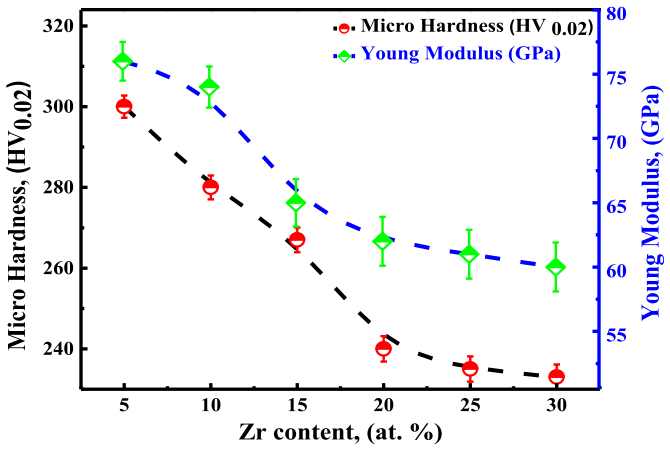

Fig. 9. Evolution of Young's modulus and Hardness of Ti–25Nb-xZr alloys with variable Zr (at. %) content.

3.3. Electrochemical characterization

3.3.1. Open circuit potential (OCP)

The OCP evolution of the Ti–25Nb-xZr alloys with different Zr contents after 1-h immersion in Ringer solution is presented over time in Fig. 10. By adding Zr, most of the OCP curves were displaced to the noblest values because passive films are forming [43,44]. The OCPs of the samples reach a stable state and are extremely close to each other after a 10-min immersion. The OCP values were −115.11, −111.43, −96.23, −72.5, −71.84, and −60.52 mv/SCE, respectively, which is in accordance with the values obtained by Ref. [45] for Ti–15Nb-xZr in Hank's solution [45,46].

A passive coating mainly consisting of ZrO_2, Nb_2O_5, or TiO_2 was formed on the homogenous corrosion surfaces of all Ti–25Nb-xZr samples [47,48]. The polarization is regulated to produce a change of Ti_2O_3 or TiO to TiO_2 (Greater stability) over 1.2 V/SCE, which increases corrosion resistance in contrast to the layers that formed spontaneously in the air [49]. Potentiodynamic polarization is responsible for the increased OCP values for the samples containing a high Zr concentration.

3.3.2. Electrochemical impedance spectroscopy (EIS) and equivalent circuit analysis

To evaluate the effect of Zr addition on the resistance of the Ti–25Nb–xZr samples to uniform corrosion, EIS measurements were performed in Ringer solution, which simulates the physiological fluid of the body. Fig. 11 presents the experimental EIS curves for Ti–30Nb-xZr (x = 5, 10, 15, 20, 25, and 30 at. %). A similar behavior of the samples in the tested environment characterizes the Bode and Nyquist diagrams.

As shown in Fig. 11a, the samples with higher Zr levels have a larger impedance modulus (Z) than the ones with lower Zr contents. The Nyquist plots in the impedance diagrams can be described by a large flat semicircle whose diameter increases with the addition of Zr. These qualitative findings, along with the impedance parameters (capacitances and resistances) displayed in Table 3, demonstrate that the Ti–25Nb-xZr system exhibits a better electrochemical behavior as the Zr content increases (see Table 4).

The Bode-magnitude plots given in Fig. 11b show that there are two separate regions. The first is at a high frequency (2.5 MHz–5 kHz), where the curves show a smooth section (slope≈0), which is due to the electrolyte response. The second range is at medium and low frequencies, where the impedance diagram has a linear slope (slope≈1), which is due to the passive film response's usual capacitive characteristic [50–52].

Three areas can be recognized in the Bode-phase plots. In the high-frequency range, the phase angle decreased to 5° with the electrolyte resistance response. In comparison, the phase angle in the medium frequency remains constant at almost 80°, which indicates a characteristic passive oxide on the surface and an almost capacitive response of the passive layer. The phase angle decreases to a small value at low frequencies due to the passive film resistance contribution [50–52].

The addition of Zr increases the frequency range above the maximum phase angle and the phase angle close to 0°, suggesting an improvement in the passive film's capacitive behavior. The important electrochemical characteristics result from the phase angle and the higher impedance [53,54]. When using simulated body fluid, increasing the Zr content

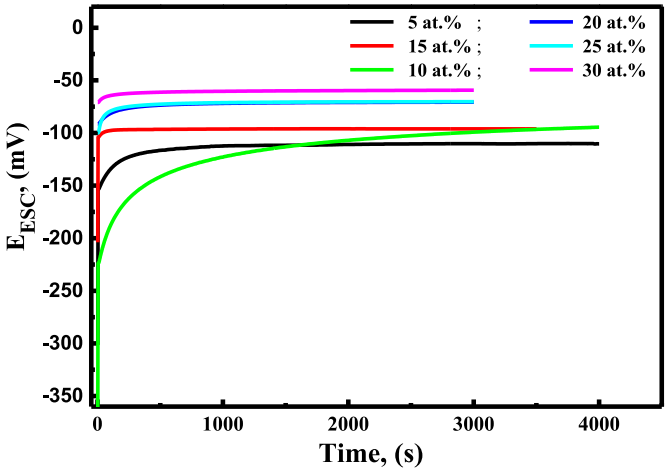

Fig. 10. The open-circuit potential of the Ti–25Nb-xZr samples vs. immersion time in ringer solution.

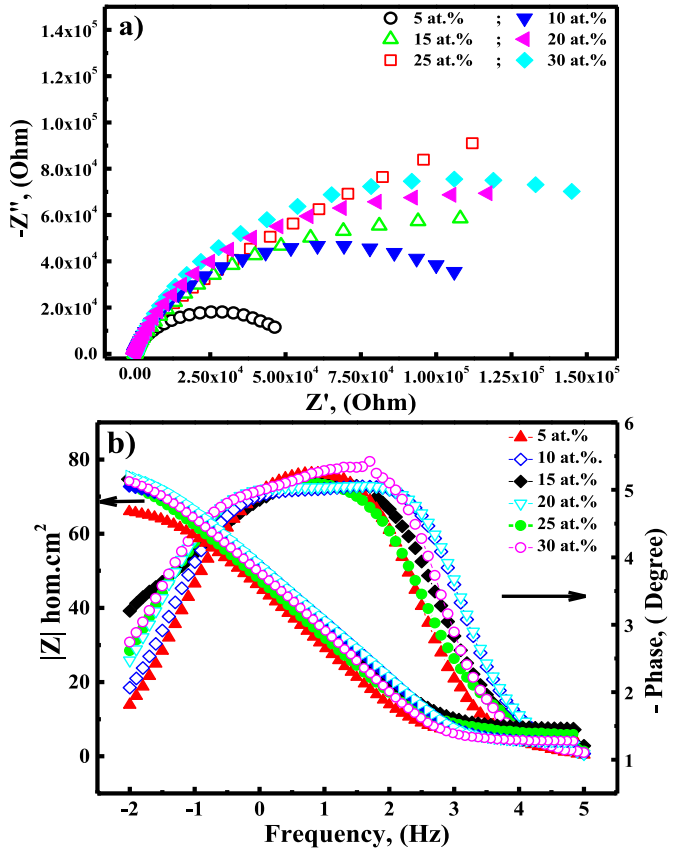

Fig. 11. The electrochemical impedance spectra of the Ti–25Nb-XZr as a function of the Zr content (at. %) after 1 h immersion in Ringer solution at 37 °C with neutral pH value 7.4, a) Nyquist plots and d) Bode plots present the impedance modulus and dephasing versus frequency.

Table 3
Impedance parameters resulting from the adaption of the equivalent circuit model fitting in Fig. 3 to the experimental EIS results in the Ringer solution.

Alloys	Rel (Ωcm^{-2})	$Z_{CPE(1)}$ (Ωcm^{-2})	n1	R1 (Ωcm^{-2}) (10^3 porous	$Z_{CPE(2)}$ (Ωcm^{-2})	n2	R2 (Ωcm^{-2}) 10^6 barrier	X^2 (10^{-4})
Ti–25Nb–5Zr	123	25 (±1.1)	0.98	0.5	28 (±1.1)	0.97	1.12	2.5
Ti–25Nb–10Zr	118	21 (±0.9)	0.99	7.1	25 (±1.3)	0.98	1.89	2.6
Ti–25Nb–15Zr	110	17 (±1.2)	0.99	16	19 (±0.6)	0.98	2.45	1.7
Ti–25Nb–20Zr	106	15(±1.0)	0.98	27	14 (±1.0)	0.99	2.87	4.01
Ti–25Nb–25Zr	95	11(±0.8)	0.99	30	13 (±0.3)	0.97	3.09	3.1
Ti–25Nb–30Zr	89	9 (±0.3)	1.0	35	12 (±0.2)	0.99	3.34	1.5

Table 4
Electrochemical parameters were extrapolated from the polarization curves I = f (E) and the corrosion speed corresponding to the Ti–25Nb-xZr surfaces (n = 5).

ALLOYS	OCP E = f(t), mV VS ECS	Potentiodynamic parameters					
		$E_{corr}/_mV$ vs ECS	I_{corr} ($\mu A.cm^2$)	βc/mV	βa/mV	V_{corr} ($mm.y^{-1}$)	RP (Ω cm^2)
Ti–25Nb–5Zr	−115.11	−410	1.40×10^{-6}	315.44	1044.8	0.144	6.26×10^4
Ti–25Nb–10Zr	111.43	−336	3.16×10^{-7}	177.5	610.5	0.0166	6.65×10^4
Ti–25Nb–15Zr	96.23	−316	3.15×10^{-7}	131.56	497.2	0.0039	8.09×10^4
Ti–25Nb–20Zr	72.5	−308	2.51×10^{-7}	148.19	375.3	0.0038	1.16×10^5
Ti–25Nb–25Zr	71.84	−246	2.32×10^{-7}	132.16	229.3	0.0029	1.30×10^5
Ti–25Nb–30Zr	60.52	−203	2.04×10^{-7}	164.64	4.90×10^6	0.0029	1.94×10^5

improves the passive film resistance of the Ti–25Nb-xZr system [55–61], as demonstrated in Fig. 13. We have already covered the importance of the suggested equivalent circuit [55–61]. The superb agreement between the fitted and experimental data means that the suggested equivalent circuit fits the experimental results nicely. This was estimated by $\chi 2 \approx 10^4$ [55] (Table 3).

The proposed equivalent circuit model (Fig. 12) is commonly utilized to fit single films on Ti-alloy surfaces [52–68]. According to the model, the oxide layer on the investigated samples is made up of an inside layer that resembles a barrier and a porous exterior layer. The parameters fitted by this model are shown in Table 3,

Where Rel represents the electrolyte resistance (Ringer's solution) at (F > 1Hz) a high-frequency limit in the Bode spectra, R2 and R1 are resistances of the barrier and the porous layer, respectively [56–60], associated with the charge transfer resistance due to the participation of the adsorbed intermediates and the porous layer (the resistances of the inner and outer layers). $Z_{CPE(1)}$ is the porous layer's capacitance, and $Z_{CPE(2)}$ is the barrier layer's capacitance, which is related to the creation of the double-layer.

For simplicity's sake, the capacitance was used as a constant phase that represented a transfer from an ultimate capacitor. The phase element impedance is uniquely described as $Z_{CPE} = [C (j\omega)n]-1$, where ω is the frequency, C is the capacitance, and $-1 \leq n \leq 1$. The non-uniform current distribution caused by surface imperfections and roughness is related to the n value [35,39]. Comparing the capacitances $Z_{CPE(1)}$ and $Z_{CPE(2)}$ of the Ti–25Nb-XZr alloys (X = 0, 5 10, 15, 20, 25, and 30 at. %) shows that the Ti–25Nb samples have higher capacitances values ($Z_{CPE(1)}$ and $Z_{CPE(2)}$ of ≈16 and 106 Ωs^{-n} cm^2 or 16 and 18μFcm^{-2}, respectively) than the Ti–25Nb–XZr (X = 5 10, 15, 20, 25, and at. 30%) alloys.

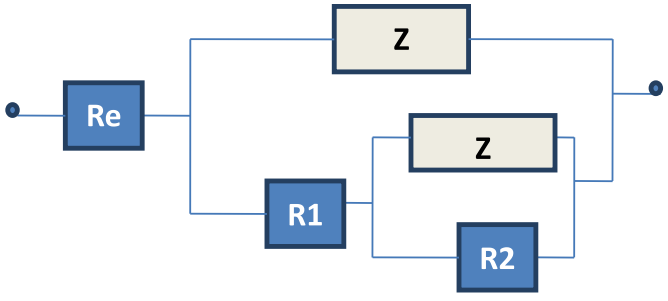

Fig. 12. Proposed equivalent circuit for fitting the impedance data for the analyzed Ti–25Nb-xZr samples in a Ringer solution.

Conversely, in the examined alloys, the polarization resistances of the porous layers (R1) are substantially lower than those of the inner barrier layer (R2). This suggests that the inner barrier layer provides the majority of the protection, as was also observed for the Ti-alloys [45,49].

The values of $Z_{CPE(2)}$ were analyzed in conjunction with the R2 values. It appears that the high phase angles at low frequencies are caused by the $Z_{CPE(2)}$ modulus. For the Ti–25Nb alloy, $Z_{CPE(1)}$ and $Z_{CPE(2)}$ are analogous (≈20 μFcm^{-2}); nevertheless, the resistance of the barrier layer (R2) is higher by a factor ≈ 103. With Zr additions, the porous layer's (ZCPE(1)) capacitance is approximately 2–20 times greater than the barrier layer's (ZCPE (2)) capacitance [5,9].

Low capacitances are linked to an increase in the passive film's thickness [69,70] and a reduction in the dielectric constant of the oxide film [61]. A more noble electrochemical corrosion behavior is attributed to the combination of high polarization resistances and low capacitances [55,58,59].

Consequently, these EIS parameters (Table 3) suggest that the addition of Zr to mechanically alloyed and milled Ti– 25Nb enhances their electrochemical behavior. They also point out that both the outer and inner film can improve corrosion protection.

As a result, polarization enhances the corrosion resistance of Ti alloys. According to the literature, the applied potential often causes the oxide film's thickness to increase [41,42]. There have also been reports of an increase in the inner barrier oxide density layer and/or the oxide film thickness [63]. The same potentiodynamic polarization behavior has been documented in binary Ti–Nb alloys owing to the production of a thicker oxide film, leading to a reduction in corrosion rates [64].

Usually, the electrochemical behavior of Ti-alloy can be enhanced mainly by adding Zr. In this research, it is observed that Zr enhances the noble properties of the alloys. It also contributes to the β-phase stabilization and provides refining of grain size.

3.3.3. *Potentiodynamic polarization results*

Fig. 13 shows experimental polarization curves in the Ringer solution for the studied samples with Zr content. The corrosion potential (E_{corr}) and the corrosion current densities (I_{Corr}) were determined by Tafel plots from the polarization curves with anodic and cathodic branches. These results confirm the tendency of the electrochemical behavior in favor of the Ti–25Nb-xZr milled alloys. The data indicates that the I_{Corr} value reduces as the Zr content increases, with Ti–25Nb exhibiting the highest value (I_{Corr}).

for all samples, The current density partially stabilizes in the range of 2 and 3 × 10^{-8} A.cm^{-2}, which is ascribed to the oxide layer's

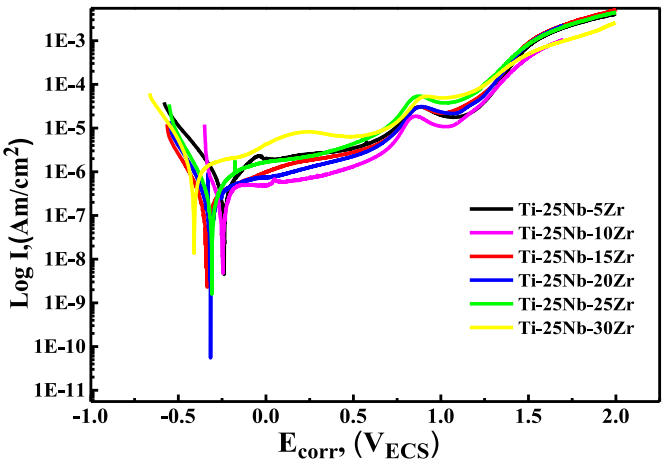

Fig. 13. Experimental polarization curves (the Ringer's solution, neutral pH, at 37 °C) for the studied systems with different Zr content (at. %).

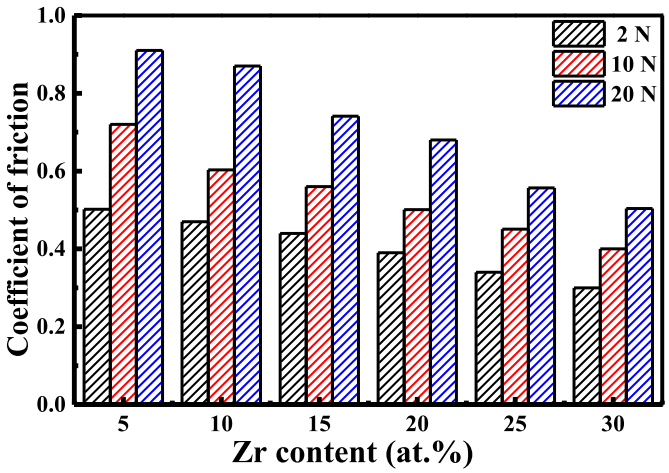

Fig. 14. Mean friction coefficients of the Ti–25Nb-xZr samples.

development. However, this oxide layer becomes steady at ≈ 0.1V. Many passive current densities (IPP) are related to the corrosion potential for every specimen. In Fig. 13, the Ti–25Nb sample shows the highest value of IPP (≈15A.cm^{-2}), the middle value of the Ti–25Nb–15Zr (≈7Acm^{-2}), and the lowest of the Ti–20Nb–30Zr samples (≈3.5 Acm^{-2}). The values of polarization (I_{Corr} and IPP) and the EIS parameters reveal the noble electrochemical behavior of the Ti–25Nb–30Zr sample compared to the samples with lower Zr content.

At potentials of 1000, 1100, 1200, 1310, 1710, and 2310 $mV_{/(SCE)}$, a breakdown passive film can be seen for Ti–25Nb–30Zr, Ti–25Nb–25Zr, Ti–25Nb–15Zr, Ti–25Nb–10Zr, Ti–25Nb–5Zr, and Ti–25Nb, respectively. While a passive Ti-oxide film is produced on the surface of the specimens, the high IPP values indicate that defects in the oxide layer can be formed with the tendency of the formation of an additional porous or irregular oxide film [66].

A stable interface in the development of bone implants is significant for dental and orthopedic applications. Several strategies have been proposed to produce positive host-implant interactions, e.g., osteoconductive coatings for implant surfaces, porous surfaces, and macroscopic irregularities (e.g., calcium phosphate coatings or hydroxyapatite) [65].

The advantages of biological porous surfaces can be increased by their ability to generate micro-mechanical bone interlocking, which results in higher implant fixation compared to a smooth surface. The bone interconnections involve slight roughness in conjunction with valleys and/or adequate shape peaks that enable bone retention and/or growth [65,66]. Porous surfaces may be helpful for the establishment of micromechanical anchoring between bone and implant and for bone ingrowth to obtain a lengthy implant lifetime.

In this research, the electrochemical tests showed that the electrochemical characteristics of the milled Ti–Nb sample significantly increase with increasing Zr addition [67]. The Ti–25Nb-XZr samples with low Zr content revealed a rougher oxide layer than other Ti–Nb–Zr samples with higher Zr content. This latter fact can be very significant for osseointegration enhancement.

3.4. Tribological characterization

Fig. 14 presents the variation of mean friction coefficients (CoF) for the Ti–25Nb-xZr samples with varying Zr contents. It can be observed that the CoF tends to reduce as the Zr content increases due to the reduction in particle and grain size reduction. The sample containing 30 at. % Zr had the lowest friction coefficient, while samples containing 10 at. % Zr had higher values. The mean values (Fig. 14) at an average load of 2 N ranged from 0.3 to 0.50. At the same time, they vary from 0.4 to 0.72 at 10 N and 0.50–0.91 at 20 N with decreasing Zr content from 35 to 10 at. %, respectively, which is also confirmed by the Hall-Petch equation ($D^{-1/2}$).

As seen in Fig. 15a, the wear volume of the Ti–Nb-xZr samples demonstrated a decreasing tendency with Zr addition from 0 to 30 at% and normal loads from 2 to 20 N. This corresponds to the reduction in wear volume of 14.3, 29.05, 41.16, 65.6, and 65.8%. As illustrated in Fig. 15b, the wear rate reduces with increasing Zr content at steady

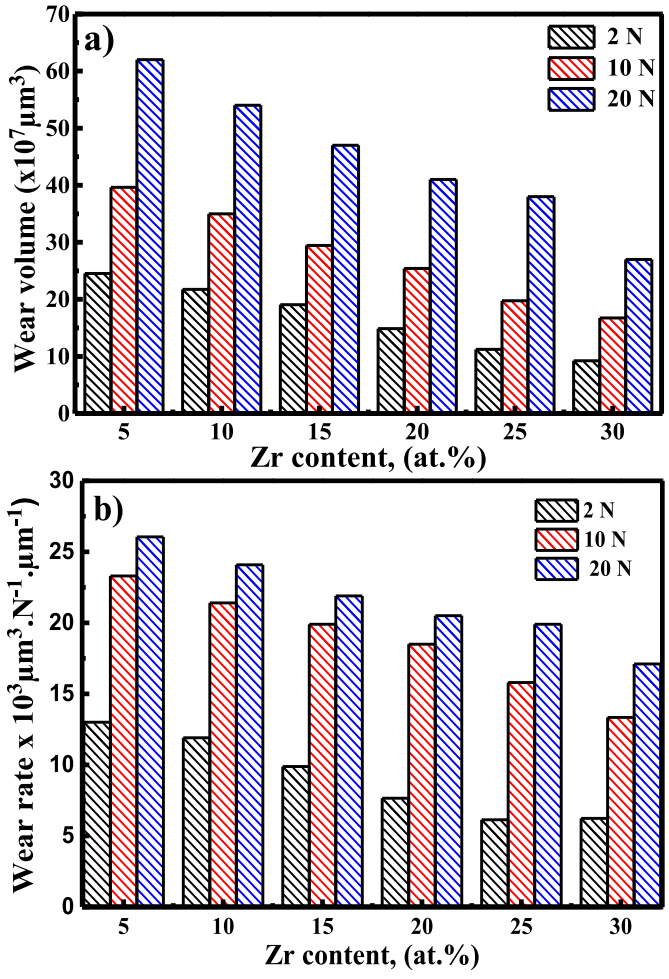

Fig. 15. Evolution of a) wear volume, b) wear rate of the Ti–25Nb-xZr alloys.

loads. In contrast, the wear rate rises as the applied load increases. It seems that the addition of Zr has an essential impact on both wear and volume rates.

Finally, wear behavior and the friction coefficient of Ti–NbZr samples depend significantly on the Zr content and the experimental conditions. As shown in Figs. 13 and 15, the β-phase Ti-alloys with 25 and 30 at% Zr (Ti–25Nb–25Zr and Ti–25Nb–30Zr) reveal good tribological behavior and high wear resistance due to the improved mechanical properties owing to grain size refinement. With increasing Zr content and load (N), wear rates and friction coefficients increase. The transfer layer was well compacted due to the frictional heat. Temporarily, both wear rate and friction were decreased by increasing the coverage area of the transfer layer. At the same time, alloys containing 30 and 35 at. % of Zr have a poorer hardness and a higher volume and wear rate when compared to alloys containing 0 to 30 at. % of Zr.

4. Conclusion

Ti–25Nb-xZr (x = 5, 10, 15, 20, 25, and 30 at. %) alloys for biomedical applications, especially for bone implants, were successfully produced by means of powder metallurgy (PM). The principle findings show that the increase in Zr content improved the microstructural properties such as lattice parameters, crystallite sizes, microstrain values, porosity, pores size, and relative density. The structural evolution of the milled alloys, morphologies, and mechanical properties were sensitive to their Zr concentration. An increase in the Zr concentration decreased the crystallite and the particle size. Both the Vickers hardness and the Young's modulus decreased with increasing Zr.

The EIS results showed the production of a single passive film on the surfaces of the alloy, and the inclusion of Zr enhanced the passive films' resistance to corrosion. The polarization curves display low corrosion current densities of the alloys with a large passive area without a breakdown of the passive films. The inclusion of Zr reduced the passive current density values and corrosion current densities. All results indicate that the titanium alloys have a nobler electrochemical activity due to the element Zr.

The addition of Zr decreased the hardness and Young's modulus while improving the wear resistance and friction of the Ti–25Nb–xZr alloys. The Ti–25Nb–30Zr alloy exhibits better tribological behavior. The alloy's friction coefficient decreased as the Zr amount increased. Considering the applications for implants, the Ti–25Nb–30Zr sample proved to be the best candidate with low material loss and Young's modulus, similar electrochemical, mechanical, and tribological behavior, and non-toxic alloying elements.

Declaration of competing interest

The authors declare that they have no known competing financial interests or personal relationships that could have appeared to influence the work reported in this paper.

Data availability

Data will be made available on the request.

Acknowledgments

The authors acknowledge the support by the german research Foundation and the BTU Cottbus-Senftenberg Germany. Also, The authors acknowledge the support received from the Researchers Supporting Project (number RSP2024R404), King Saud University, Riyadh, Saudi Arabia.

References

[1] D. Marwa, M. Fellah, H. Hezil, M. Benoudia, A. Obrosov, M. Abdul Samad, Structural and mechanical evaluation of a new Ti-25Nb-25Mo alloy produced by high-energy ball milling with variable milling time for biomedical applications, Int. J. Adv. Manuf. Technol. (2023), https://doi.org/10.1007/s00170-023-12650-0.

[2] D. Wang, X. Wang, M.L. Jin, P. He, S. Zhang, Molecular level manipulation of charge density for solid-liquid TENG system by proton irradiation, Nano Energy 103 (2022) 107819, https://doi.org/10.1016/j.nanoen.2022.107819.

[3] O. Mazigi, M.B. Kannan, J. Xu, H.C. Choe, Q. Ye, Biocompatibility and degradation of a low elastic modulus Ti–35Nb–3Zr alloy: nanosurface engineering for enhanced degradation resistance, ACS Biomaterials Science and Engeneering 3 (2017) 509–517, https://doi.org/10.1021/acsbiomaterials.6b00563.

[4] D. Liao, S. Zhu, B. Keshtegar, G. Qian, Q. Wang, Probabilistic framework for fatigue life assessment of notched components under size effects, Int. J. Mech. Sci. 181 (2020) 105685, https://doi.org/10.1016/j.ijmecsci.2020.105685.

[5] M. Fellah, N. Hezil, M.A. Hussein, M. Abdul Samad, M.Z. Touhami, A. Montagne, A. Iost, A. Obrosov, S. Weiss A, Preliminary investigation on the bio-tribocorrosion behaviour of porous nanostructured β-type titanium based biomedical alloy, Materials Lettres 257 (2019) 126755.

[6] M.T. Mohammed, Z.A. Khan, M. Geetha, Effect of thermo-mechanical processing on microstructure and electrochemical behavior of Ti–Nb–Zr–V new metastable β titanium biomedical alloy, Trans. Nonferrous Metals Soc. China 25 (2015) 759–769, https://doi.org/10.1016/S1003-6326(15)63661-5.

[7] M. Fellah, N. Hezil, D. Bouras, A. Obrosov, M. Abdul Samad, A. Montagne, S. Weiß, Structural, mechanical and tribological performance of a nano structured biomaterial Co-Cr-Mo alloy synthesized via mechanical alloying, J. Mater. Res. Technol. 25 (2023) 2152–2165.

[8] X. Zhang, W. Ye, L. Mushongera, Y. Liao, Unravelling heterogeneities in sub-grain cellular structure and micromechanical response of additive manufactured Ti-Nb alloys, Addit. Manuf. 59 (2022) 103146, https://doi.org/10.1016/j.addma.2022.103146.

[9] M. Fellah, N. Hezil, M.Z. Touhami, M. Abdul Samad, A. Obrosov, D.O. Bokov, A. M. Alhussein, Structural, tribological and antibacterial properties of (α+ β) based ti-alloys for biomedical applications, J. Mater. Res. Technol. 9 (6) (2020) 14061–14074.

[10] M. Karanjai, R. Sundaresan, G.V.N. Rao, T. R Mohan, B.P. Kashyap, Development of titanium based biocomposite by powder metallurgy processing with in situ forming of Ca–P phases, Materials Science and Engineering: A 447 (2007) 19–26, https://doi.org/10.1016/j.msea.2006.10.154.

[11] R. Karre, M.K. Niranjan, S.R. Dey, First principles theoretical investigations of low Young's modulus beta Ti–Nb and Ti–Nb–Zr alloys compositions for biomedical applications, Mater. Sci. Eng. C 50 (2015) 52–58, https://doi.org/10.1016/j.msec.2015.01.061.

[12] M. Fellah, N. Hezil, M.Z. Touhami, A. Obrosov, W. Sabine, E.B. Kashkarov, A. Iost, Enhanced structural and tribological performance of nanostructured Ti–15Nb alloy for biomedical applications", Results Phys. 15 (2019) 102767.

[13] A. Biesiekierski, J. Wang, M.A. Gepreel, C. Wen, A new look at biomedical Ti-based shape memory alloys, Acta Biomater. 8 (2012) 1661–1669, https://doi.org/10.1016/j.actbio.2012.01.018.

[14] T. Lee, S. Lee, I.-S. Kim, Y.H. Moon, H.S. Kim, C.H. Park, Breaking the limit of Young's modulus in low-cost Ti–Nb–Zr alloy for biomedical implant applications, J. Alloys Compd. 828 (2020) 154401, https://doi.org/10.1016/j.jallcom.2020.154401.

[15] X. Li, S. Zhu, D. Liao, J.A.F.O. Correia, F. Berto, Q. Wang, Probabilistic fatigue modelling of metallic materials under notch and size effect using the weakest link theory, Int. J. Fatig. 159 (2022) 106788, https://doi.org/10.1016/j.ijfatigue.2022.106788.

[16] F. Hamadi, M. Fellah, N. Hezil, D. Bouras, S. E Laouini, M. Alex, A.E.-K. Hamiden, A. Obrosov, G.A. El-Hiti, Krishna Kumar Yadav, Effect of milling time on structural, physical and tribological behavior of a newly developed Ti-Nb-Zr alloy for biomedical applications, Adv. Powder Technol. 35 (1) (2024), https://doi.org/10.1016/j.apt.2023.104306.

[17] P. Chui, R. Jing, F. Zhang, J. Li, T. Feng, Mechanical properties and corrosion behavior of β-type Ti-Zr-Nb-Mo alloys for biomedical application, J. Alloys Compd. 842 (2020) 155693, https://doi.org/10.1016/j.jallcom.2020.155693.

[18] N. Hezil, M. Fellah, Synthesis, structural and mechanical properties of nanobioceramic (α-Al_2O_3)", Journal of the Australian Ceramic Society 55 (2019) 1167–1175.

[19] S. Guo, Q. Meng, X. Zhao, Q. Wei, H. Xu, Design and fabrication of a metastable β-type titanium alloy with ultralow elastic modulus and high strength, Sci. Rep. 5 (2015) 14688.

[20] E.D. Gonzalez, N.K. Fukumasu, C.R.M. Afonso, P. Nascente, Impact of Zr content on the nanostructure, mechanical, and tribological behaviors of β-Ti-Nb-Zr ternary alloy coatings, Thin Solid Films 721 (2021) 138565, https://doi.org/10.1016/j.tsf.2021.138565.

[21] Q.D. Martins, W.R. Osorio, M.E.P. Souza, R. Caram, A. Garcia, Effects of Zr content on microstructure and corrosion resistance of Ti–30Nb–Zr casting alloys for biomedical applications, Electrochim. Acta 53 (2008) 2809–2817, https://doi.org/10.1016/j.electacta.2007.10.060.

[22] J. Málek, F. Hnilica, J. Veselý, B. Smola, K. Kolařík, J. Fojt, M. Vlach, V. Kodetová, The effect of Zr on the microstructure and properties of Ti-35Nb-XZr alloy, Materials Science and Engineering: A 675 (2016) 1–10, https://doi.org/10.1016/j.msea.2016.07.069.

[23] Y. Cui, Y. Li, K. Luo, H. Xua, Microstructure and shape memory effect of Ti–20Zr–10Nb alloy, Materials Science and Engineering: A 527 (2010) 652–656, https://doi.org/10.1016/j.msea.2009.08.063.

[24] Y.P. Hou, S. Guo, X.L. Qiao, T. Tian, Q.K. Meng, X.N. Cheng, X.Q. Zhao, Origin of ultralow Young's modulus in a metastable β-type Ti–33Nb–4Sn alloy, Journal of the mechanical behavior of biomedical materials 59 (2016) 220–225, https://doi.org/10.1016/j.jmbbm.2015.12.037.

[25] M. Fellah, N. Hezil, L. Dekhil, M. Abdul Samad, R. Djellabi, S. Kosman, A. Montagne, A. Iost, A. Obrosov, S. Weiss, Effect of sintering temperature on structure and tribological properties of nanostructured Ti−15Mo alloy for biomedical applications, Trans. Nonferrous Met. Soc. China 29 (11) (2019) 2310–2320.

[26] J. Liu, Y. Zhou, J. Lu, R. Cai, T. Zhao, Y. Chen, Y. Chen, Y. Injectable, Tough and adhesive zwitterionic hydrogels for 3D-printed wearable strain sensors, Chem. Eng. J. 475 (2023) 146340, https://doi.org/10.1016/j.cej.2023.146340.

[27] F. Hammadi, M. Fellah, N. Hezil, L. Aissani, M. Guessem, S. Mechachti,M. Abdul Samad, A. Montagne, A. Iost, S. Wiess, A. Obrosov, The effect of milling time on the microstructure and mechanical properties of Ti-6Al-4Fe alloys, Materials today communication. 27(1), 102428 https://doi.org/10.1016/j.mtcomm.2021.102428..

[28] S. Fu, H. Wu, W. He, Q. Li, C. Shan, J. Wang, C. Hu, Conversion of dielectric surface effect into volume effect for high output energy, Adv. Mater. 35 (40) (2023) 2302954, https://doi.org/10.1002/adma.202302954.

[29] D.R.N. Correa, P.A.B. Kuroda, M.L. Lourenço, M.A.R. Buzalaf, C.R. Grandini, Adjustment of the microstructure and selected mechanical properties of biomedical Ti-15Zr-Mo alloys through oxygen doping, J. Alloys Compd. 775 (2019) 158–167, https://doi.org/10.1016/j.jallcom.2018.10.105.

[30] N. Boucharebi, N. Hezil, M. Fellah, F. Hamadi, Effect of milling time on structural, mechanical and tribological behavior of a newly developed Ti-Ni alloy for biomedical, Material Today communication (2024), https://doi.org/10.1016/j.mtcomm.2024.108201.

[31] S.V. Grib, A.G. Illarionov, A.A. Popov, O.M. Ivasishin, Development and investigation of the structure and physical and mechanical properties of lowmodulus Ti-Zr-Nb alloys, Phys. Met. Metallogr. 115 (2014) 600–608, https://doi.org/10.1134/S0031918X14030041.

[32] C. Yang, C. Yin, Y. Wu, Q. Zhou, X. Liu, Atomic insights into the deformation mechanism of an amorphous wrapped nanolamellar heterostructure and its effect on self-lubrication, J. Mater. Res. Technol. 26 (2023) 4206–4218, https://doi.org/10.1016/j.jmrt.2023.08.215.

[33] C. Ning, D. Ding, K. Dai, W. Zhai, L. Chen, The effect of Zr content on the microstructure, mechanical properties and cell attachment of Ti–35Nb–xZr alloys, Biomedical Materials 5 (2010) 045006, https://doi.org/10.1088/1748-6041/5/4/045006.

[34] C. Zhou, Z. Ren, Y. Lin, Z. Huang, L. Shi, Y. Yang, .J. Mo, Hysteresis dynamic model of metal rubber based on higher-order nonlinear friction (HNF), Mech. Syst. Signal Process. 189 (2023) 110117, https://doi.org/10.1016/j.ymssp.2023.110117.

[35] Y. Ren, J. Du, B. Liu, Z.B. Jiao, Y. Tian, I. Baker, H. Wu, Microstructure, mechanical properties and biocompatibility of laser metal deposited Ti–23Nb coatings on a NiTi substrate, Materials Science and Engineering: A 848 (2022) 143402, https://doi.org/10.1016/j.msea.2022.143402.

[36] X.H. Yan, J. Ma, Y. Zhang, High-throughput screening for biomedical applications in a Ti-Zr-Nb alloy system through masking co-sputtering, Sci. China Phys. Mech. Astron. 62 (2019) 1–9, https://doi.org/10.1007/s11433-019-9387-7.

[37] K. Pramod, G.S. Mahobia, S. Mandal, V. Singh, E. Chattopadhyay, Corrosion resistance of the surface modified Ti-13Nb-13Zr alloy by ultrasonic shot peening, Corrosion Sci. 189 (2021) 109597, https://doi.org/10.1016/j.corsci.2021.109597.

[38] M. Fellah, N. Hezil, M.Z. Touhami, A. Obrosov, S. Weiß, E.B. Kashkarov, A. Iost, Enhanced structural and tribological performance of nanostructured Ti-15Nb alloy for biomedical applications, Results Phys. 15 (2019) 102767, https://doi.org/10.1016/j.rinp.2019.102767.

[39] A.L.R. Ribeiro, P. Hammer, L.G. Vaz, L.A. Rocha, Are new TiNbZr alloys potential substitutes of the Ti-6Al-4V alloy for dental applications? An electrochemical corrosion study, Biomedical Materials 8 (2013) 65005, https://doi.org/10.1088/1748-6041/8/6/065005.

[40] M. Farah, M. Fellah, D. Bouras, N. Hezil, A. Becheri, B. Regis, H. Daoudi, A. Montagne, A. Tmader, A.W.K. Hamiden, Unraveling the role of sintering temperature on physical, structural and tribological characteristics of ball milled Co28Cr6Mo biomaterial based alloy, Journal of engineering research (2023), https://doi.org/10.1016/j.jer.2023.10.040.

[41] X. Long, K. Chong, Y. Su, C. Chang, L. Zhao, Meso-scale low-cycle fatigue damage of polycrystalline nickel-based alloy by crystal plasticity finite element method, Int. J. Fatig. 175 (2023) 107778, https://doi.org/10.1016/j.ijfatigue.2023.107778.

[42] M.W. Mendes, C.G. Ágreda, A.H. Bressiani, J.C. Bressiani, A new titanium based alloy Ti-27Nb-13Zr produced by powder metallurgy with biomimetic coating for use as a biomaterial, Mater. Sci. Eng. C 63 (2016) 671–677.

[43] M. Dahmani, M. Fellah, N. Hezil, M.-C. Benoudia, M.A. Samad, A. Alburaikan, H. A. El-Wahid Khalifa, A. Obrosov, Structural and mechanical evaluation of a new Ti-25Nb-25Mo alloy produced by high-energy ball milling with variable milling time for biomedical applications, Int. J. Adv. Manuf. Technol. 129 (2023) 1–21, https://doi.org/10.1007/s00170-023-12650-O.

[44] B. Xie, H. Li, Y. Ning, M. Fu, Discontinuous dynamic recrystallization and nucleation mechanisms associated with 2-, 3- and 4-grain junctions of polycrystalline nickel-based superalloys, Mater. Des. 231 (2023) 112041, https://doi.org/10.1016/j.matdes.2023.112041.

[45] S. Gao, H. Li, H. Huang, R. Kang, Grinding and lapping induced surface integrity of silicon wafers and its effect on chemical mechanical polishing, Appl. Surf. Sci. 599 (2022) 153982, https://doi.org/10.1016/j.apsusc.2022.153982.

[46] B. Yuan, B. Yang, Y. Gao, M. Lai, X.H. Chen, M. Zhu, Achieving ultra-high superelasticity and cyclic stability of biomedical Ti–11Nb–4O (at.%) alloys by controlling Nb and oxygen content, Mater. Des. 92 (2016) 978–982, https://doi.org/10.1016/j.matdes.2015.12.148.

[47] M.A. Hussein, M. Kumar, R. Drew, N. Al-Aqeeli, Electrochemical corrosion and in vitro bioactivity of nano-grained biomedical Ti-20Nb-13Zr alloy in a simulated body fluid, Materials 11 (2018) 1–15, https://doi.org/10.3390/ma11010026.

[48] W. Xu, J. Tian, Z. Liu, X. Lu, M.D. Hayat, Y. Yan, Z. Li, X. Qu, C. Wen, Novel porous Ti-35Zr-28Nb scaffolds fabricated by powder metallurgy with excellent osteointegration ability for bone-tissue engineering applications, Mater. Sci. Eng. C 105 (2019) 110015, https://doi.org/10.1016/j.msec.2019.110015.

[49] J. Hu, Y. Ren, Q. Huang, H. He, L. Luxin, J. Liu, R. Li, H. Wu, Microstructure and corrosion behavior of Ti-Nb coatings on NiTi substrate fabricated by laser cladding, Coatings 11 (2021) 597, https://doi.org/10.3390/coatings11050597.

[50] X. Yi, B. Huang, W. Gao, B. Sun, X. Feng, X. Cao, Y. Guo, X. Meng, Z. Gao, H. Wang, Damping behaviors and strain recovery characteristics of Hf-modified TiNb-based shape memory alloys, Mater. Res. Bull. 158 (2023) 112084, https://doi.org/10.1016/j.materresbull.2022.112084.

[51] W. Kuang, H. Wang, X. Li, J. Zhang, Q. Zhou, Y. Zhao, Application of the thermodynamic extremal principle to diffusion-controlled phase transformations in Fe-C-X alloys: modeling and applications, Acta Mater. 159 (2018) 16–30, https://doi.org/10.1016/j.actamat.2018.08.008.

[52] J. Wang, Z. Pan, Y. Wang, L. Wang, L. Su, D. Cuiuri, H. Li, Evolution of crystallographic orientation, precipitation, phase transformation and mechanical properties realized by enhancing deposition current for dual-wire arc additive manufactured Ni-rich NiTi alloy, Addit. Manuf. 34 (2020) 101240, https://doi.org/10.1016/j.addma.2020.101240.

[53] E.S. Leva, J.B. Fogagnolo, R.B. Falcão, J.B.F. Neto, C.T.D. Santos, D.L. Bayerlein, F. J.G. Landgraf, Processing of Ti–13Nb–13Zr powder by selective laser melting under a relatively high oxygen atmosphere, J. Manuf. Process. 79 (2022) 259–269, https://doi.org/10.1016/j.jmapro.2022.04.065.

[54] C. Aguilar, E. Pio, A. Medina, C. Parra, R. Mangalaraja, P. Martin, I. Alfonso, K. Tello, Effect of Sn on synthesis of nanocrystalline Ti-based alloy with fcc structure, Trans. Nonferrous Metals Soc. China 30 (2020) 2119–2131, https://doi.org/10.1016/S1003-6326(20)65365-1.

[55] C. Cayron, Shifting the shear paradigm in the crystallographic models of displacive transformations in metals and alloys, Crystals 8 (2018) 181, https://doi.org/10.3390/cryst8040181.

[56] E.R. Baek, G. Suprobo, Massive phase transformation as a new perspective on microstructural design in a titanium alloy-A review, Mater. Sci. Forum 1000 (2020) 428–435. https://doi.org/10.4028/www.scientific.net/MSF.1000.428.

[57] M. Fellah, N. Hezil, F. Hamadi, A. Iqbal, M.A. Samad, A. Alburaikan, H. Abd El-Wahed khalifa, O. Aleksei, Effect of Fe content on physical, tribological and photocatalytical properties of Ti-6Al-xFe alloys for biomedical applications, Tribol. Int. 191 (2024) 109146, https://doi.org/10.1016/j.triboint.2023.109146.

[58] G. Rajender, P.K. Giri, Strain induced phase formation, microstructural evolution and bandgap narrowing in strained TiO_2 nanocrystals grown by ball milling, J. Alloys Compd. 676 (2016) 591–600, https://doi.org/10.1016/j.jallcom.2016.03.154.

[59] B.B. Zhang, B.L. Wang, Y.B. Wang, L. Li, Y.F. Zheng, Y. Liu, Development of Ti-Ag-Fe ternary titanium alloy for dental application, J. Biomed. Mater. Res. B 100B (2012) 185–196, https://doi.org/10.1002/jbm.b.31937.

[60] A. Balyanov, J. Kutnyakova, N.A. Amirkhanova, V.V. Stolyarov, R.Z. Valiev, X. Z. Liao, Y.H. Zhao, Y.B. Jiang, H.F. Xu, T.C. Lowe, Y.T. Zhu, Corrosion resistance of ultra fine-grained Ti, Scripta Mater. 51 (2004) 225–229, https://doi.org/10.1016/j.scriptamat.2004.04.011.

[61] M. Niinomi, Metallic biomaterials, Journal Artif Organs 11 (2008) 105–110, https://doi.org/10.1007/s10047-008-0422-7.

[62] M. Fellah, N. Hezil, M. Abdul Samad, R. Djellabi, A. Montagne, A. Mejias, S. Weiss, Effect of Molybdenum content on structural, mechanical, and tribological properties of hot isostatically pressed β-type titanium alloys for orthopedic applications, J. Mater. Eng. Perform. 28 (10) (2019) 5988–5999.

[63] H. Fouzia, M. Fellah, N. Hezil, L. Aissani, M. Goussem, M. Said, A.S. Mohammed, A. Montagne, I. Alain, S. Weiss, A. Obrosov, The effect of milling time on the microstructure and mechanical properties of Ti-6Al-4Fe alloys, Mater. Today Commun. 27 (2021) 102428, https://doi.org/10.1016/j.mtcomm.2021.102428.

[64] M.M.M. López, J. Faure, M.A.E. Medina, M.I.E. Cabrera, M.E.C. García, Enhanced corrosion resistance in artificial Saliva of Ti6Al4V with ZrO_2 nanostructured coating, J. Electrochem. Soc. 162 (2015) 3090–3100, https://doi.org/10.1149/2.0231511jes.

[65] Z. Qin, X. Pang, L. Qiao, M. Khodayari, A.A. Volinsky, Water molecules effect on pure Ti passive film structure in methanol solution, Appl. Surf. Sci. 303 (2014) 282–289, https://doi.org/10.1016/j.apsusc.2014.02.167.

[66] S. Kumar, T.S.N. Sankara Narayanan, S.S. Kumar, Influence of fluoride ion on the electrochemical behaviour of β-Ti alloy for dental implant application, Corrosion Sci. 52 (2010) 1721–1727, https://doi.org/10.1016/j.corsci.2010.01.008.

[67] Y. Sasikumar, M. Karthega, R. Nallaiyan, In vitro bioactivity of surface-modified β-Ti alloy for biomedical applications, J. Mater. Eng. Perform. 20 (2011) 1271–1277, https://doi.org/10.1007/s11665-010-9772-4.
[68] H. Bouchemel, A. Benchettara, "Corrosion behavior of a new Ti–3Mo alloy in simulated body fluid for biomedical applications", Arabian J. Sci. Eng. 39 (2014) 139–146.
[69] W. Kong, E.M. Francis, Q. Shi, S. C Cox, F. Wang, M. Kuang, M.M. Attallah, The influence of advanced hot isostatic pressing on phase transformations, mechanical properties of Ti-34Nb-13Ta-5Zr-0.2O alloy manufactured by in-situ alloying via selective laser melting, J. Alloys Compd. 903 (2022) 163974, https://doi.org/10.1016/j.jallcom.2022.163974.
[70] T. Tao, D. Zhou, J. Liu, X. Wang, Improvement of laser welded joint properties of AZ31B magnesium alloy to DP590 dual-phase steel produced by external magnetic field, J. Manuf. Process. 79 (2022) 270–283, https://doi.org/10.1016/j.jmapro.2022.04.069.